Magnetic bio-activated carbons production using different process parameters for phosphorus removal from artificially prepared phosphorus-rich and domestic wastewater

Yuming Wen, Zhaoran Zheng, Shule Wang, Tong Han, Weihong Yang, Pär Göran Jönsson

Chemosphere 271 (2021) 129561

Contents lists available at ScienceDirect

Chemosphere

journal homepage: www.elsevier.com/locate/chemosphere

Magnetic bio-activated carbons production using different process parameters for phosphorus removal from artificially prepared phosphorus-rich and domestic wastewater

Yuming Wen [a], Zhaoran Zheng [a, b], Shule Wang [a], Tong Han [a, *], Weihong Yang [a], Pär Göran Jönsson [a]

[a] KTH Royal Institute of Technology, Department of Materials Science and Engineering; Brinellvägen 23, 114 28 Stockholm, Sweden
[b] BGRIMM Technology Group, 100160 Beijing, China

HIGHLIGHTS

- Magnetic bio-activated carbons were produced from lignin and $FeSO_4$.
- Optimized process uses wet impregnation and 16 g/(h*g(lignin)) steam flow rate.
- The highest maximum phosphorus adsorption capacity reaches 69.80 mg-P/g.
- Representative MBAC significantly removed phosphorus from domestic wastewater.

GRAPHICAL ABSTRACT

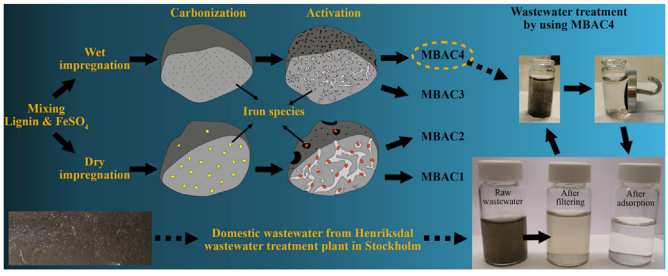

ARTICLE INFO

Article history:
Received 18 October 2020
Received in revised form
15 December 2020
Accepted 18 December 2020
Available online 7 January 2021

Handling Editor: Yongmei Li

Keywords:
Bio-activated carbon
Phosphorus adsorption
Wastewater treatment

ABSTRACT

A series of magnetic bio-activated carbon (MBAC) has been produced from lignin and ferrous salts following to the process including impregnation, carbonization, and steam activation. The influence of the impregnation methods and the steam flow rate on the quality and the maximum phosphorus adsorption capacity of the produced MBACs has been investigated. The phosphorus adsorption performance in real domestic wastewater of the MBAC with the highest maximum phosphorus adsorption capacity has been investigated. The results show that all of the produced MBACs have a relatively rich porous structure, and all surface iron species exist as magnetite (Fe_3O_4). Compared with the MBACs that are produced via the dry impregnation method using a lower steam flow rate, the MBACs that are produced via the wet impregnation method using a higher steam flow rate are believed to have a higher iron content and better iron species dispersion. The highest maximum phosphorus adsorption capacity of all the produced MBACs is estimated to be as high as 69.80 mg-P/g according to the best-fitting Langmuir model. The MBAC that shows the highest maximum phosphorus adsorption capacity could also remove 84.65% and 96.97% of the total phosphorus from the filtered raw domestic wastewater (FRDW) and treated domestic wastewater (TDW), respectively, which indicates a good potential for using MBACs for domestic wastewater treatment.

1. Introduction

Due to phosphorus enrichment, domestic wastewater always

* Corresponding author. Brinellvägen 23, 114 28 Stockholm, Sweden.
E-mail address: tongh@kth.se (T. Han).

https://doi.org/10.1016/j.chemosphere.2021.129561

suffers from the eutrophication problem, which has been recognized as a major problem that is not conducive to the sustainable and non-toxic development of the world (Nyenje et al., 2010). Nowadays, chemical precipitation of phosphorus by using metal salts such as $FeSO_4$ and $Al_2(SO_4)_3$ is the most widely used phosphorus removal technology in domestic wastewater treatment plants (Bunce et al., 2018). Two main issues are debatable when considering the sustainability of this technology. The first one is that excess chemicals, i.e., metal salts, need to be used to obtain the solubility product of the metal phosphorus (Wilfert et al., 2015). As the phosphorus is removed, new metal ions and corresponding anions are introduced into the domestic wastewater (Desmidt et al., 2015). The second issue is that in the subsequent conversion and utilization of wastewater sludges, additional processes are needed for the recovery of metal phosphorus (Gherghel et al., 2019; Luyckx et al., 2020). An inquiry to propose a ban on spreading sewage sludge on farmland and a phosphorus recycling requirement has been published by the Swedish government in 2018 ((Inquiry to propose ban on, 2018)).

Using green adsorbents to adsorb phosphorus and developing a corresponding suitable reuse process for saturated adsorbents are believed to be ideal solutions (Qambrani et al., 2017; Bacelo et al., 2020). Magnetic bio-activated carbon (MBAC) is one of the most promising green adsorbents for phosphorus adsorption (Li et al., 2020). On the one hand, MBAC has the advantages of being rapidly separated from the water system via a magnet and having an enhanced phosphorus adsorption capacity due to the electrostatic adsorption between the surface decorated metal oxides and phosphorus. On the other hand, saturated MBACs have been reported to be used as potential soil fertilizers to provide plants with the required phosphorus (Li et al., 2016).

A streamlined process of producing MBACs by using lignin and $FeSO_4$ as raw materials was initially proposed in our previous work, which combined carbon and iron species via lignin melting properties and oxidized iron species to form magnetite via the injection of steam. The maximum phosphorus adsorption capacity of the representative MBAC, which was produced according to the proposed process, was estimated to be 21.14 mg/g (Han et al., 2020a). Notably, the focus of the previous study is the streamlined process proposal and verification. A more detailed study focusing on the investigation of the influence of the process parameters such as iron loading, iron addition methods, and steam flow rate is missing. The maximum phosphorus adsorption capacity of the produced MBAC is believed to be significantly improved after a detailed parameter optimization study, which led to the current study.

Moreover, most of the existing research investigates the phosphorus adsorption performance of MBACs by using simulated wastewater. Only limited studies investigated the phosphorus adsorption performance of the produced MBACs for real wastewater. For example, Cai et al. attempted to use MBAC produced from water hyacinth to reclaim phosphorus from eutrophic water collected from Lake Dianchi, China, in which ~94% of phosphorus was removed when the MBAC concentration reached 5 g/l (Cai et al., 2017). However, research about using MBACs for phosphorus adsorption from domestic wastewater is needed, which is a research gap and is of interest to study.

In this work, a series of MBACs was produced. The influence of different process parameters is studied. The mass ratio of $FeSO_4$/lignin used in this study is twice that used in the previous study (Han et al., 2020a). Moreover, two different $FeSO_4$ impregnation methods, i.e., dry impregnation and wet impregnation, and two different steam flow rates, i.e., 4 g/(h*g(char)) and 8 g/(h*g(char)), are used. The textural properties, iron contents, iron compound valences, and surface chemistry of the produced MBACs are characterized via performing N_2 adsorption-desorption, Inductively Coupled Plasm Atomic Emission Spectroscopy (ICP-AES), XRD, and X-ray Photoelectron Spectroscopy (XPS) analyses. Phosphorus adsorption isotherms of the MBACs are obtained via fitting the saturation adsorption data obtained for simulated phosphorus solutions with different concentration gradients to Langmuir and Freundlich models. The maximum phosphorus adsorption capacity of the MBACs is estimated according to the best-fit model. The MBAC with the highest maximum phosphorus adsorption capacity is further used for phosphorus adsorption in real domestic wastewater.

2. Materials and methods

2.1. Materials

Kraft lignin produced from spruce by using the CleanFlow Black process (Abbadessa et al., 2018) is applied as the carbon source. Before the experiment, the lignin was first dried at room temperature to a moisture content of ~2%. After that, the dried lignin was grinded and sieved to the size of $d < 0.125$ mm.

Guaranteed reagent graded ferrous salt ($FeSO_4$) was purchased from Sigma-Aldrich to act as a magnetic component precursor. $FeSO_4$ was grinded and sieved to a size range similar to that of the prepared lignin ($d < 0.125$ mm).

The ultimate and proximate analysis results of lignin and $FeSO_4$ can be found in (Han et al., 2020a).

2.2. Production of the MBACs

Prior to the experiment, 3.8 g $FeSO_4$ is added to 10 g lignin by using two different impregnation methods, i.e., dry impregnation and wet impregnation. For the dry impregnation method, lignin and $FeSO_4$ are directly mechanically mixed without involving any liquid. For the wet impregnation method, lignin is added into the $FeSO_4$ solution, which is produced via dissolving 3.8 g $FeSO_4$ into 69.5 ml distilled water. The resulting solid-liquid mixture is magnetically stirred at room temperature for 6 h to make $FeSO_4$ adhere better to the surface of lignin. Then, the solid-liquid mixture is put into the drying oven to dry overnight.

In the current work, MBACs are produced by mainly using a horizontal tubular furnace. The flow chart of the furnace and corresponding accessories is shown in Fig. 1. $FeSO_4$-impregnated lignin samples are first put in a silica boat, which is subsequently placed into the furnace tube for a carbonization process. During the carbonization process, samples are slowly heated to a temperature of 600 °C in a nitrogen atmosphere at a heating rate of 10 °C and held at this temperature for 1 h. The flow rate of nitrogen is set as 50 ml/min. After this, the samples are further heated in the nitrogen atmosphere to a temperature of 800 °C, which is the most applied gasification temperature (Han et al., 2020b), for the subsequent steam activation process. When the temperature of the samples reaches 800 °C, the nitrogen supply is switched off, and the water supply is switched on. The flow rate of the supplied water is controlled by using a peristaltic pump. In this work, two different water flow rates, i.e., 2 and 4 g/(h*g(lignin)), are used. The duration time of steam injection is fixed as 1 h. The biochar yield of the lignin pyrolysis process fluctuates at approximately 50% (Zhang et al., 2020). In this way, the steam-to-char ratios are approximately 4 and 8. Before entering the furnace, water with a fixed flow rate will first pass through a steam generator to be preheated to a temperature around 250 °C. A detailed description of the performed cases, the definitions, and the yield rates of the MBAC products obtained in this work have been shown in Table 1.

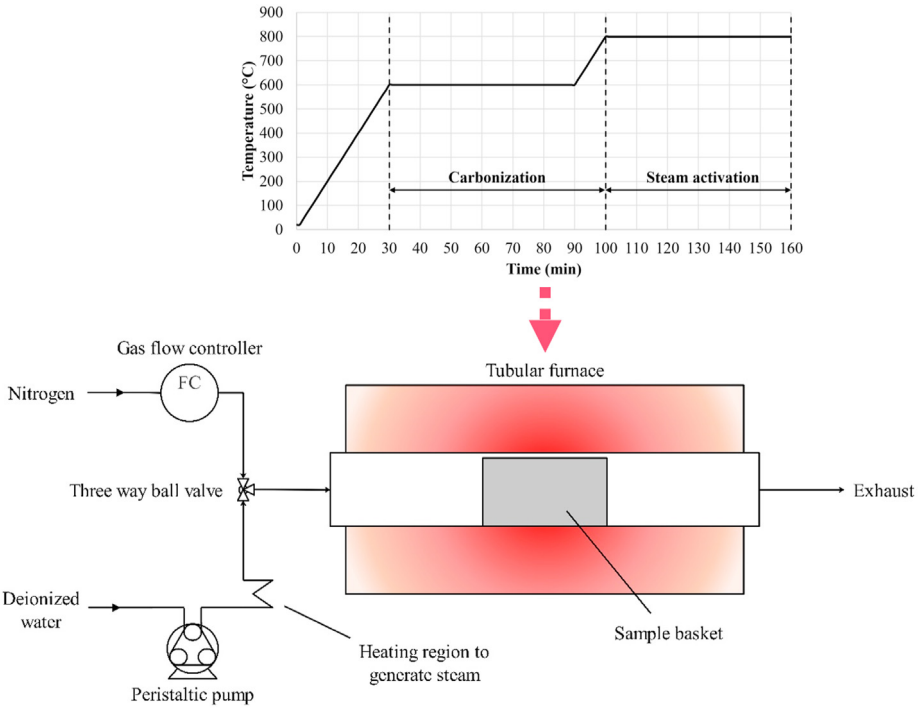

Fig. 1. Schematic layout of the experimental setup.

Table 1
Production process of the different MBAC samples.

Raw materials	Carbonization	Steam activation	Definition	Yield rate
10 g lignin +3.8 g $FeSO_4$ Dry impregnation	600 °C, 50 ml/min N_2, 1 h	800 °C, 2 g/(h*g(lignin)) steam, 1 h	MBAC1	37.5 wt%
10 g lignin +3.8 g $FeSO_4$ Dry impregnation	600 °C, 50 ml/min N_2, 1 h	800 °C, 4 g/(h*g(lignin)) steam, 1 h	MBAC2	26.3 wt%
10 g lignin +3.8 g $FeSO_4$ Wet impregnation	600 °C, 50 ml/min N_2, 1 h	800 °C, 2 g/(h*g(lignin)) steam, 1 h	MBAC3	30.0 wt%
10 g lignin +3.8 g $FeSO_4$ Wet impregnation	600 °C, 50 ml/min N_2, 1 h	800 °C, 4 g/(h*g(lignin)) steam, 1 h	MBAC4	16.9 wt%

wt.%: weight percent.

2.3. Characterization

The textural properties of the MBACs were determined by using a Micromeritics model ASAP 2000 instrument to obtain nitrogen adsorption-desorption isotherms at 77 K. The surface area (S_{BET}) and average pore radius (APR) were calculated by using the BET equation. The micropore volume ($V_{Micropore}$) and the pore size distributions in the micropore range were determined by the Horvath and Kawazoe (KH) method. The mesopore volume ($V_{Mesopore}$) and the pore size distributions in the mesopore range were determined by calculations using density functional theory (DFT). The total pore volume (TPV) is obtained by adding $V_{Micropore}$ and $V_{Mesopore}$ together.

ICP-AES was performed to determine the iron contents of the MBACs. Before being placed into the ICP-AES instrument for characterization of the iron contents, the produced MBACs were firstly placed in a 200 ml HCl solution with a pH = 2 for 2 h, and then, the acid-treated MBACs were dissolved by using a microwave digestion instrument.

XRD was performed to determine the crystal structure of the MBACs. A Siemens D5000 diffractometer and a monochromatic Cu Kα radiation source (30 mA, 40 kV) were used to characterize the crystallographic phases of the produced MBACs over the 2θ range of 10−90° with a step size of 0.02°/s.

XPS was used to characterize the chemical composition of the surface of the MBAC samples. XPS analysis was performed on a Thermo-Fisher ESCALAB250Xi instrument. The binding energies were calibrated to the common C1s peak at 284.6 eV. Peak differentiation and fitting analysis were performed via XPS peak 41 software.

The magnetic hysteresis loops of MBAC4 were measured by using a vibrating sample magnetometer (VSM). During the experiment, more than 40 mg of MBAC4 was loosely packed. Afterward, the measurement was performed with an applied magnetic field between −20 kOe to 20 kOe and with a step size of 10 Oe.

The concentrations of the total phosphorus (C_{TP}) and ammoniacal nitrogen (C_{AN}) of the solutions were measured by using a portable multi-parameter detector (LH-C3) from Hangzhou Lohand Biological Co. Ltd. Prior to the C_{TP} measurements, the solutions were decomposed at 150/165 °C for 15 and 20 min by using a decomposer (XC-200) from Hangzhou Lohand Biological Co. Ltd.

2.4. Phosphorus adsorption experiments

In this work, MBACs have been used for two different types of wastewater treatment. One type of treatment uses simulated

phosphorus solutions that are prepared by dissolving KH_2PO_4 into deionized water; the other type of treatment uses real domestic wastewater collected from Stockholm Vatten och Avfall AB. The C_{TP} and C_{AN} values of the solutions are measured by using a portable multi-parameter detector (LH-C3) from Hangzhou Lohand Biological Co. Ltd. Prior to the C_{TP} measurement, the solutions were decomposed at 150 °C for 15 min by using a decomposer (XC-200) from Hangzhou Lohand Biological Co. Ltd.

The phosphorus adsorption capacities of all the produced MBACs are measured by using simulated phosphorus solutions with different concentration gradients. Phosphorus solutions with different concentrations (5, 10, 25, 50, 100, and 500 mg/L) were prepared by dissolving a specific amount of KH_2PO_4 in distilled water. The initial pH of the phosphorus solutions was then adjusted to 7 by adding the 1 mol/L NaOH solution. For each adsorption experiment, 0.4 g MBAC samples are put into a 60 ml simulated phosphorus solution. The mixtures were then subjected to mechanical agitation for 24 h at room temperature.

The MBAC with the highest maximum phosphorus adsorption capacity is further used for phosphorus adsorption in real domestic wastewater. Real wastewater from two different treatment stages have been collected from Stockholm Vatten och Avfall AB. One wastewater sample is raw domestic wastewater without any treatment. For this kind of wastewater, a filtration process is conducted first to remove all solids in the water. The other wastewater sample is domestic wastewater collected after the filtration, pre chemical precipitation, and bio-digestion processes. This wastewater can be discharged into nature after a second chemical precipitation process, which is used to further lower the phosphorus concentration below the allowed minimum phosphorus concentrations of emissions. The raw domestic wastewater obtained after filtration is denoted as filtered raw domestic wastewater (FRDW), and the domestic wastewater that can be discharged into nature after a second chemical precipitation process is denoted as treated domestic wastewater (TDW).

For the phosphorus adsorption tests performed on both FRDW and TDW, 0.8 g of the tested MBAC samples are put into 120 ml of wastewater. The C_{TP} of the FRDW and TDW has been measured after the samples were treated for periods of times of 0, 1, 2, 3, 4, and 5 h under constant mechanical agitation at room temperature. Moreover, the C_{AN} values of the FRDW/TDW and the 5 h-treated FRDW/TDW sample were also measured.

3. Result and discussion

3.1. Characterization of the MBAC samples

3.1.1. Textural properties

The textural properties of the produced MBAC samples are listed in Table 2. It can be seen that the porous properties of the MBACs that were produced via dry impregnation (MBAC1 and 2) are different from those of the MBACs that were produced via wet impregnation (MBAC3 and 4). Moreover, the porous properties of the MBACs that are produced via the same impregnation methods also vary due to the usage of different steam-to-char ratios.

For the MBACs that are produced via the dry impregnation method, MBAC1 has a surface area value as high as 645.83 m^2/g, which is also the highest among the surface areas of all the produced MBACs. MBAC2 has a surface area value that is approximately 100 m^2/g lower than that of MBAC1. Moreover, the micropore volume of MBAC2 is lower than that of MBAC1. It is known that the steam-to-char ratio used for MBAC2 production is twice that used for MBAC1 production. According to the literature, the surface area and micropore volumes of the activated carbons produced via the steam activation of char exhibited maximum values at an intermediate char burn-off rate of approximately 50% (Chang et al., 2000). As the char burn-off rate further increases, both the micropore volume and the specific surface area will decrease due to the excessive consumption of carbon. Therefore, the different char burn-off rates caused by the different steam-to-char ratios seem to be the main reason that causes the different porous properties of MBAC1 and MBAC2. However, the mesopore volumes of MBAC1 and MBAC2 are all extremely low, which is not as expected. The existence of a relatively high percentage of iron species seems to be the main reason.

Table 2
Textural properties of the MBACs.

	MBAC1	MBAC2	MBAC3	MBAC4
S_{BET} (m^2/g)	645.83	543.24	379.84	586.88
TPV (cm^3/g)	0.27	0.22	0.18	0.25
$V_{Micropore}$ (cm^3/g)	0.26	0.22	0.16	0.24
$V_{Mesopore}$ (cm^3/g)	0.01	0.00	0.02	0.01

However, for the MBACs produced via the wet impregnation method, the surface area (586.88 m^2/g) and the micropore volume (0.24 cm^3/g) of MBAC4 are both higher than those of MBAC3 (379.84 m^2/g and 0.16 cm^3/g, respectively). The result indicates that MBAC4 is produced after a char burn-off rate that is closer to 50%. The steam-to-char ratio used for MBAC4 production is also twice that used for MBAC3 production. Therefore, it seems that the $FeSO_4$ impregnation methods also significantly influence the porous properties of the produced MBACs. Compared to the activation process of the dry impregnation method, the wet impregnation method seems to cause a steam activation process with a much lower char burn-off rate when the same steam-char-ratio is used. The difference in the $FeSO_4$ particle sizes and dispersion caused by the different impregnation methods is believed to be the decisive factor. The $FeSO_4$ that is added to lignin via the wet impregnation method is believed to have a smaller particle size and better dispersion than the $FeSO_4$ that is added to lignin via the dry impregnation method. As a result, during the steam activation process, iron species would cover the produced char's surface more uniformly and obstruct contact between the char and steam more seriously during the wet impregnation method than during the dry impregnation method. This will inevitably cause a reduction in the char burn-off rate. Moreover, the mesopore volumes of MBAC3 and MBAC4 are also extremely low. This may further indicate that the existence of a relatively high percentage of iron species limits the development of mesopores.

The pore size distributions of the MBACs are given in Fig. 2. It can be seen that the pore size of the MBACs that are produced via dry impregnation (MBAC1 and MBAC2) mainly concentrates in a range from 1.1 nm to 1.7 nm. The pore volume of MBAC2 in the pore size range between 1.1 and 1.3 nm is lower than that of MBAC1. However, the pore volume of MBAC2 in the pore size range between 1.3 and 1.7 nm is higher than that of MBAC1. The higher char burn-off rate caused by the higher steam-to-char ratio during MBAC2 production is believed to be the main reason (Satya Sai and Krishnaiah, 2005). This clearly indicates the pore widening effect of steam at a relatively high steam char burn-off rate. The pore size of the MBACs that are produced via wet impregnation (MBAC3 and MBAC4) mainly concentrates in a range from 1.1 nm to 1.4 nm. The pore volume of MBAC3 in the whole pore size range is significantly lower than that of MBAC4. This is believed to be caused by a high primary char-burn off stage during MBAC3 production. By combining all these results, it can be concluded that the pore size distributions of the MBACs are consistent with their textural property analysis results.

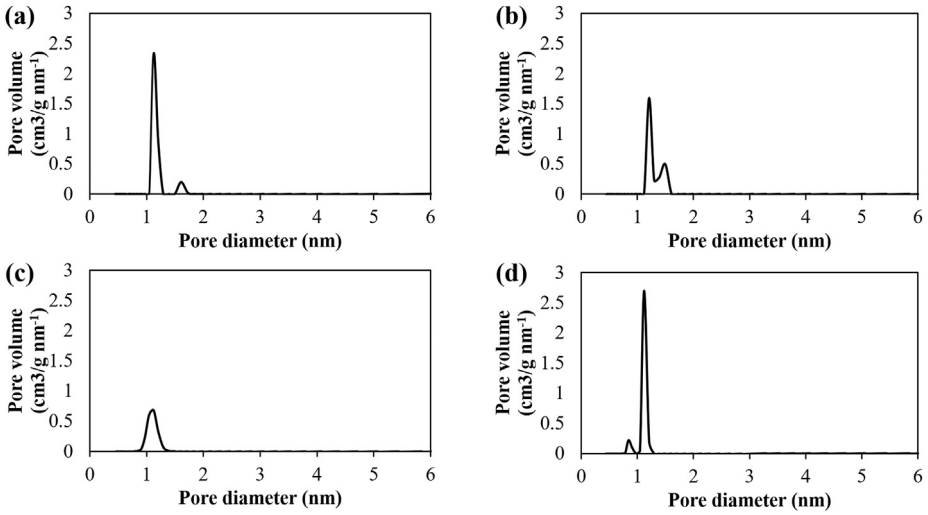

Fig. 2. The pore size distribution of the MBACs: (a) MBAC1, (b) MBAC2, (c) MBAC3, and (d) MBAC4.

3.1.2. Iron forms and iron content

The XRD patterns of the produced MBACs are shown in Fig. 3. It can be seen that all the MBACs exhibit almost the same XRD patterns. This indicates that the iron species on all the MBACs exist in the same state. As marked in Fig. 3, the observed peaks that are detected at 2θ of 0.076°, 35.426°, 43.053°, 53.411°, 56.935°, and 62.520° are confirmed to correspond to the (220), (311), (400), (422), (511), and (400) crystal planes of Fe_3O_4, respectively. Moreover, peaks belonging to the crystal phases of other iron species, such as Fe and Fe_2O_3, are difficult to observe. All these results indicate that all the iron species on all the MBACs exist as Fe_3O_4. The results are consistent with the conclusions obtained from our previous study: ferrous salt is buried in the carbon matrix during the lignin melting process. Then, the ferrous salt is decomposed and reduced to Hagg iron carbide (Fe_5C_2) during the carbonization process. Finally, Hagg iron carbide (Fe_5C_2) is exposed and oxidized to form magnetite (Fe_3O_4) during the steam activation process. Steam is not only an activation agent for pore generation and widening but is also effective for the oxidization of Fe_5C_2 to form Fe_3O_4 (Han et al., 2020a).

It is difficult to determine the difference between the iron contents of the different MBACs by evaluating the XRD patterns due to their difficulty of being quantified. Therefore, the iron contents of the MBACs are further determined by using ICP-AES techniques. The iron content of MBAC2 (15.68%) is around 1.5% lower than that of MBAC1 (17.07%). This suggests that during the steam activation of the biochar produced after the carbonization of $FeSO_4$-dry impregnated lignin, significant iron loss occurs during char burn-off. The result is contrary to the results obtained from the previous work, which concluded that almost no iron was lost during the steam activation process (Han et al., 2020a). The use of twice the amount of $FeSO_4$ ought to be the main reason. However, the difference between the iron contents of MBAC3 and MBAC4 is quite obvious. The iron content of MBAC4 (41.17%) is more than two times that of MBAC3 (16.80%). This result indicates that, during the steam activation of the biochar produced after the carbonization of $FeSO_4$-wet impregnated lignin, the iron loss is quite small. Combining all these results, it can be concluded that different impregnation methods also lead to different degrees of iron loss during the steam activation process. Compared to the dry impregnation method, the wet impregnation method causes much less iron loss during the steam activation process. This is probably contributed by the better dispersion of the iron species on the surface by using the wet impregnation method, which integrates the iron content and the char more firmly.

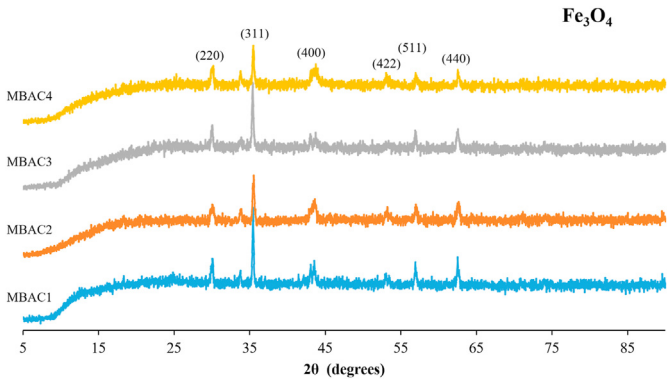

Fig. 3. XRD patterns of MBACs.

3.1.3. Surface chemistry

XPS analyses have been performed to detect the surface functional groups of the MBACs. Survey scans from 800 to 200 eV are presented in Fig. S1 for all four samples. It can be seen that three main elements, i.e., carbon, oxygen, and iron, are detected on the surface of all the MBACs samples. This is as expected, since these three types of elements are the main components of MBACs. Specifically, as C is the most abundant element, the surface atomic percentage of carbon is estimated to be approximately 90.37%, 87.05%, 87.22%, and 79.96% for MBAC1, MBAC2, MBAC3, and MBAC4, respectively. Moreover, no extra obvious peaks were detected, suggesting that the ash contents of all the produced MBACs ought to be relatively low (Zhang et al., 2013).

To further reveal the detailed chemical forms of the surface of the samples, high-resolution XPS (HR-XPS) analysis was performed on the Fe 2p and C 1s. To identity the chemical state of Fe, XPS is one of the best characterization methods as it is extraordinarily sensitive to the cations of Fe^{3+} and Fe^{2+} (Lu et al., 2010). The typical Fe 2p spectra, curve fits, and individual curves associated with the different iron states are shown in Fig. S2. It can be seen that for all MBACs, iron species are present as Fe^{3+} or Fe^{2+}. No iron species existing as other states such as Fe^0 can be detected. Moreover, the areas under the curves corresponding to Fe^{3+}, which is a direct

indicator of its content, are obviously bigger than that those under the curves corresponding to Fe^{2+}. All these results are in consistent with the XRD results and further confirm that all the iron species in all the MBACs exist as Fe_3O_4.

The proportions of carbon in the different chemical states with respect to the total amount of carbon existing on the surfaces of the MBACs are obtained by determining the contribution of the areas under the curves for each carbon state to the total area under the C 1s curve. The typical C 1s spectra, curve fits and individual curves associated with the different carbon states are shown in Fig. S3. Due to the influence of neighbouring atoms, the peak positions representing the same functional states of carbon are slightly different for the different samples (Burke et al., 1992). The results show that four different functional states of carbon, i.e., hydrocarbons (C-H and C-C), hydroxyls or ethers (C-O), carbonyls (C=O) and carboxylic acids or esters (O-C=O), are present on the surface of all the MBACs.

The proportions of carbon in different chemical states with respect to the total amount of carbon existing on the surfaces of all the MBACs were obtained by determining the contribution of the areas under the curves for each carbon state to the total area under the C 1s curve. The results are shown in Table S1. It can be seen that, for all the MBACs, approximately 45%–55% of all carbons bond with oxygen, resulting in the formation of carbon-oxygen functional groups. The result indicates that all the MBACs exhibit a good surface chemistry, as is expected. According to the literature, during the steam gasification process, H_2O would dissociate into O or O-containing radicals on the char surface. While H radicals would combine to form H_2 and desorb from chars, O-containing species could react with char to form various O-containing complexes (Zhang et al., 2011).

3.2. Adsorption of phosphorus

3.2.1. Phosphorus adsorption performance of MBACs for simulated phosphorus solutions

The phosphorus adsorption data of the MBACs have been obtained by using the simulated phosphorus solutions with different concentration gradients. The Langmuir model (1) and the Freundlich model (2) are then applied to fit the experimental data by using MATLAB Curve Fitting Toolbox 3.5.9. Herein, the Langmuir model assumes monolayer adsorption onto a homogeneous surface without further interaction between adsorbed molecules; the Freundlich model is an empirical model, which illustrates non-ideal multilayer chemisorption on a heterogeneous surface (Li et al., 2020).

$$q_e = \frac{K_L Q C_e}{1 + K C_e} \quad (1)$$

$$q_e = k_F C_e^{\,n} \quad (2)$$

where.

q_e: the equilibrium amount of phosphorus adsorbed on the adsorbent (mg/g);
C_e: the equilibrium concentration of phosphorus in solution (mg/L);
Q: the maximum monolayer coverage capacity (mg/g);
K_L: the Langmuir isotherm constant (L/mg);
K_F: the Freundlich isotherm constant (mg/g);
n: the heterogeneity factor.

The isotherm data and model-fittings of the simulated phosphorus adsorption onto the MBACs are shown in Fig. 4, the parameters deduced from the Langmuir and Freundlich models, are listed in Table 3. It can be seen that, for all the MBACs except

Table 3
Parameters of simulated phosphorus adsorption onto MBACs, as deduced from the Langmuir and Freundlich models.

Sample	Model	K	Q	N	R^2
MBAC1	Langmuir	1.1×10^{-3}	27.51	–	0.9961
	Freundlich	0.14	–	0.66	0.9815
MBAC2	Langmuir	2.6×10^{-3}	29.20	–	0.8766
	Freundlich	0.49	–	0.53	0.7759
MBAC3	Langmuir	2.2×10^{-4}	46.80	–	0.9875
	Freundlich	0.03	–	0.80	0.9927
MBAC4	Langmuir	3.7×10^{-4}	69.80	–	0.9917
	Freundlich	0.09	–	0.76	0.9959

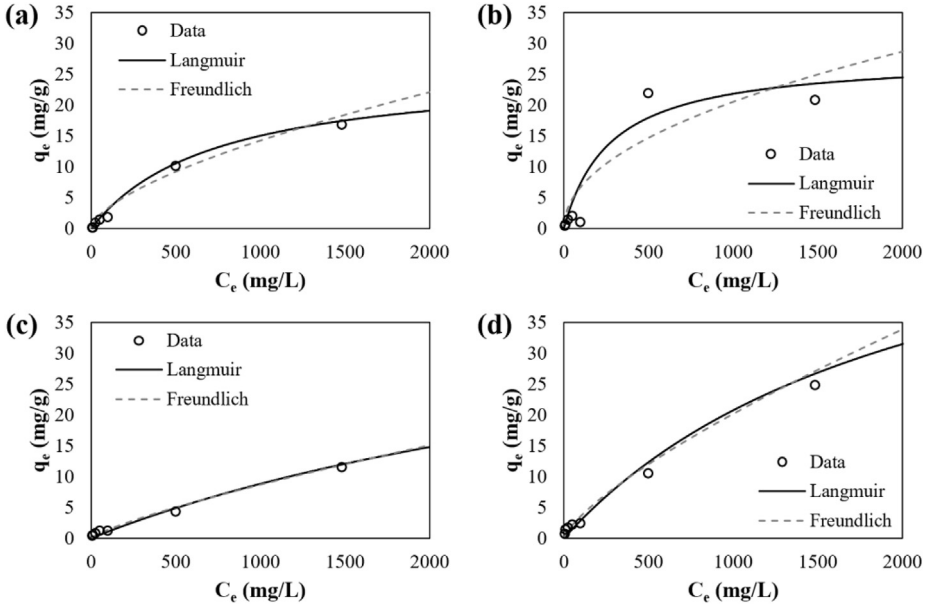

Fig. 4. Isotherm data and modelling of phosphorus adsorption onto MBACs: (a) MBAC1, (b) MBAC2, (c) MBAC3, and (d) MBAC4.

MBAC2, both the Langmuir and Freundlich models reproduced the isotherm data well, with correlation coefficients (R^2) higher than 0.98. For MBAC2, the Langmuir model reproduced the isotherm data, with correlation coefficients (R^2) of approximately 0.8766, which is better than the R^2 of the Freundlich model, with correlation coefficients (R^2) of approximately 0.7759. Therefore, the adsorption between phosphorus and MBACs ought to follow the Langmuir adsorption model. In this way, Q could represent the maximum phosphorus adsorption capacity for all the MBACs. From Table 3, it can be seen that the maximum phosphorus adsorption capacity of MBAC3 and MBAC4, which are produced via the wet impregnation method, are much higher than that of MBAC1 and MBAC2, which are produced via the dry impregnation method. MBAC4 shows the highest maximum phosphorus adsorption capacity among all the produced MBACs, which is as high as 69.80 mg-P/g. This result is a significant increase from the result obtained in our previous work. In our previous work, the maximum phosphorus adsorption capacity of the tested MBAC sample was estimated to be 21.18 mg/g (Han et al., 2020a). Moreover, compared with the maximum phosphorus adsorption capacities of most magnetic biochars and MBACs reported in the literature (Chen et al., 2011; Long et al., 2011; Yan et al., 2015; Li et al., 2016; Cai et al., 2017; Michálková-Richveisová et al., 2017; Zhang et al., 2017; Wang et al., 2019), this number is much higher. All these results indicate the good utilization potential of MBAC4.

3.2.2. Domestic wastewater treatment and its phosphorus adsorption kinetics

As mentioned before, MBAC4, the MBAC exhibiting the highest maximum phosphorus adsorption capacity among all the produced MBACs, is further used to adsorb water-soluble phosphorus in FRDW and TDW. The results are listed in Table 4. It can be seen that, for both FRDW and TDW, C_{TP} drops rapidly during the first h of treatment and then decreases slowly. Specifically, the C_{TP} of FRDW and TDW decreases from 7.23 mg/l to 3.63 mg/l and from 0.33 mg/l to 0.03 mg/l, respectively. In addition, after 5 h of treatment, the C_{TP} of FRDW and TDW stabilizes at values of approximately 1.11 mg/l and 0.01 mg/l, respectively. The results indicate a total phosphorus removal efficiency equal to 84.65% and 96.97% for FRDW and TDW, respectively. All these results indicate that MBAC4 is effective for the removal of water-soluble phosphorus in domestic wastewater. Meanwhile, the C_{AN} of FRDW and TDW stabilizes at values of approximately 38.32 mg/l (decreases from 57.48 mg/l) and 11.27 mg/l (decreases from 19.54 mg/l), respectively.

Two commonly used mathematical models, i.e., pseudo-first-order (Eq. (4)) and pseudo-second-order (Eq. (5)) models, are further used to simulate the adsorption kinetics. MATLAB Curve Fitting Toolbox 3.5.9 is applied for curve fitting. The fit curves are shown in Fig. 5. The parameters deduced for the two models are listed in Table 5.

Table 4
C_{TP} and C_{AN} of two domestic wastewaters versus the adsorption time of MBAC4.

Time (h)	FRDW C_{TP} (mg/L)	TDW C_{TP} (mg/L)	FRDW C_{AN} (mg/L)	TDW C_{AN} (mg/L)
0	7.23	0.33	57.48	19.54
1	3.63	0.03	–	–
2	3.33	0.02	–	–
3	2.71	0.01	–	–
4	2.03	0.02	–	–
5	1.11	0.01	38.32	11.27

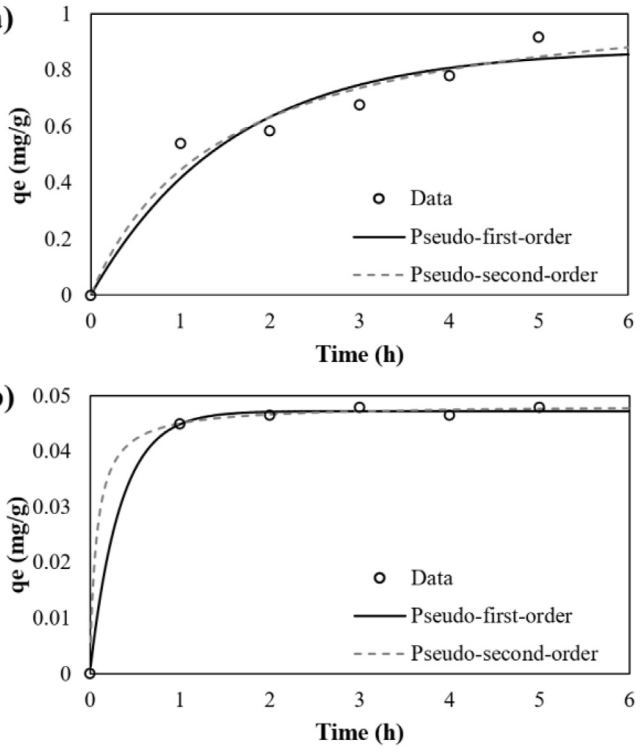

Fig. 5. Kinetics fitting results of the phosphorus adsorption uptake on MBAC4 for different domestic wastewater samples: (a) FRDW; (b) TDW.

Table 5
Best-fit parameter results of the models of the kinetics data for FRDW and TDW.

	Model	k	q_e	R^2
FRDW	Pseudo-first-order	$k_1 = 0.64$	0.88	0.9542
	Pseudo-second-order	$k_2 = 0.62$	1.10	0.9695
TDW	Pseudo-first-order	$k_1 = 3.00$	0.05	0.9986
	Pseudo-second-order	$k_2 = 277.10$	0.05	0.9988

$$q_t = q_e\left(1 - e^{-k_1 t}\right) \quad (4)$$

$$q_t = \frac{q_e^2 k_2 t}{1 + q_e k_2 t} \quad (5)$$

where.

q_e: the amount of phosphorus adsorbed on the adsorbent at equilibrium (mg/g);
q_t: the amount of phosphorus adsorbed on the adsorbent at time t (mg/g);
k_1: the adsorption rate constant of the pseudo-first-order model (h^{-1});
k_2: the adsorption rate constant of the pseudo-second-order model (g mg^{-1} h^{-1}).

The pseudo-first-order model is often used for reversible reactions in which equilibrium is reached between the solid and the liquid phases (Qiu et al., 2009). In contrast, the pseudo-second-order model is preferred for chemisorption processes, where the adsorbate and adsorbent act as covalent forces (Ho and McKay, 1999). As shown in Fig. 5, both models fit well with the adsorption data. In addition, the majority of phosphorus is adsorbed during the initial 1 h. From Table 5, it can be seen that, for FRDW,

the pseudo-second-order model, with correlation coefficients (R^2) of 0.9695, fits the adsorption data slightly better than the pseudo-first-order model, with correlation coefficients (R^2) of 0.9542. This result suggests that the rate-limiting step could be the chemical sorption between phosphorus and Fe_3O_4 on the surface of MBAC4 (Vikrant et al., 2018). For TDW, due to the relatively low initial C_{TP} (0.33 mg/g), both the pseudo-first-order model and the pseudo-second-order model fit the adsorption data extremely well, with correlation coefficients (R^2) higher than 0.998.

Notably, unlike the simulated phosphorus solutions, real domestic wastewater inevitably has a large number of other coexisting ions, such as SO_4^{2-} and NO_3^-. The ammonia and nitrogen concentration of approximately 20% for the real domestic wastewater, as shown in Table 4, also supports this. The adsorption competition between these ions and phosphorus is important to know when considering the utilization of MBACs for domestic wastewater treatment (Hollister et al., 2013). From the kinetic analysis results, it has been concluded that the majority of phosphorus is adsorbed during the initial 1 h, and the rate-limiting phosphorus adsorption step could be chemical sorption between phosphorus and Fe_3O_4 on the surface of MBAC4. It seems that the influence of the coexisting ions on the adsorption of phosphorus by using MBAC4 is negligible for the domestic wastewater investigated in the current work.

Photos of domestic wastewaters collected during different treatment stages have been shown in Fig. 6. It can be seen that the raw domestic wastewater collected from the wastewater treatment plant is a turbid liquid with a large amount of suspended black solid. After the solids were filtered away, the colour of the liquid is still turbid. However, after MBAC treatment and further separation, the colour of the liquid becomes clear and transparent. This result indicates that the use of MBAC4 could increase the clarity of wastewater. In addition, from Fig. 6, it can also be seen that the MBAC4 powders can be easily attracted to a magnet, which indicates the good magnetic property of MBAC4. The magnetic hysteresis curve of MBAC4, which can also be found in Fig. 6, also support this result.

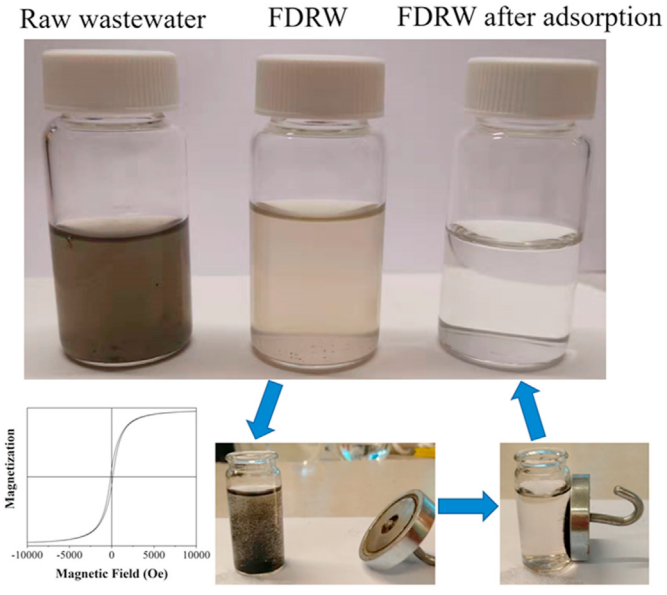

Fig. 6. Pictures of domestic wastewaters collected during different treatment stages by using MBAC4 and the magnetic response of MBAC4.

4. Conclusions

A series of MBACs has been prepared according to processes including impregnation, carbonization, and steam activation by using lignin and ferrous salts as raw materials. The influence of the impregnation method and the steam flow rate on the quality of the produced MBACs has been investigated. The characterization results indicate that all the produced MBACs have a relatively rich porous structure, and all the surface iron species exist as magnetite (Fe_3O_4). Compared with the MBACs that are produced via the dry impregnation method, the MBACs that are produced via the wet impregnation method are believed to have higher iron content and better iron species dispersion. The phosphorus adsorption capacity of all the produced MBACs has been measured by using simulated phosphorus-rich solutions with different concentrations. The Langmuir adsorption model was confirmed to be the best-fitting model of adsorption between the MBACs and phosphorus. The highest maximum phosphorus adsorption capacity of all the produced MBACs is estimated to be as high as 69.80 mg-P/g. The MBAC that shows the highest phosphorus adsorption capacity was further used for phosphorus removal in domestic wastewater, and the results indicate that 84.65% and 96.97% of the total phosphorus could be removed from FRDW and TDW by a 5 h treatment, respectively, and that the rate-limiting step could be chemical sorption between phosphorus and Fe_3O_4 on the surface of the MBAC.

Declaration of competing interest

The authors declare that they have no known competing financial interests or personal relationships that could have appeared to influence the work reported in this paper.

Acknowledgements

The financial support from FORMAS-Swedish Research Council for Sustainable Development under water JPI program is highly acknowledged. Shule Wang and Tong Han would like to acknowledge the financial support from the China Scholarship Council (CSC).

Appendix A. Supplementary data

Supplementary data to this article can be found online at https://doi.org/10.1016/j.chemosphere.2021.129561.

Credit author statement

Yuming Wen: Investigation, Formal analysis, Writing - Original Draft, Writing - Review & Editing, Visualization. **Zhaoran Zheng**: Investigation, Formal analysis. **Shule Wang**: Writing - Review & Editing. **Ton Han**: Conceptualization, Methodology, Investigation, Formal analysis, Writing - Original Draft, Writing - Review & Editing. **Weihong Yang**: Writing - Review & Editing, Supervision. **Pär Göran Jönsson**: Writing - Review & Editing, Supervision.

References

Abbadessa, A., Oinonen, P., Henriksson, G., 2018. Characterization of two novel bio-based materials from pulping process side streams: ecohelix and CleanFlow black lignin. BioResources 13, 7606–7627.
Bacelo, H., Pintor, A.M., Santos, S.C., Boaventura, R.A., Botelho, C.M., 2020. Performance and prospects of different adsorbents for phosphorus uptake and recovery from water. Chem. Eng. J. 381, 122566.
Bunce, J.T., Ndam, E., Ofiteru, I.D., Moore, A., Graham, D.W., 2018. A review of phosphorus removal technologies and their applicability to small-scale domestic wastewater treatment systems. Front. Environ. Sci. 6, 8.
Burke, G.M., Wurster, D.E., Berg, M.J., Veng-Pedersen, P., Schottelius, D.D., 1992.

Surface characterization of activated charcoal by X-ray photoelectron spectroscopy (XPS): correlation with phenobarbital adsorption data. Pharmaceut. Res. 9, 126–130.
Cai, R., Wang, X., Ji, X., Peng, B., Tan, C., Huang, X., 2017. Phosphate reclaim from simulated and real eutrophic water by magnetic biochar derived from water hyacinth. J. Environ. Manag. 187, 212–219.
Chang, C.-F., Chang, C.-Y., Tsai, W.-T., 2000. Effects of burn-off and activation temperature on preparation of activated carbon from corn cob agrowaste by CO2 and steam. J. Colloid Interface Sci. 232, 45–49.
Chen, B., Chen, Z., Lv, S., 2011. A novel magnetic biochar efficiently sorbs organic pollutants and phosphate. Bioresour. Technol. 102, 716–723.
Desmidt, E., Ghyselbrecht, K., Zhang, Y., Pinoy, L., Van der Bruggen, B., Verstraete, W., Rabaey, K., Meesschaert, B., 2015. Global phosphorus scarcity and full-scale P-recovery techniques: a review. Crit. Rev. Environ. Sci. Technol. 45, 336–384.
Gherghel, A., Teodosiu, C., De Gisi, S., 2019. A review on wastewater sludge valorisation and its challenges in the context of circular economy. J. Clean. Prod. 228.
Han, T., Lu, X., Sun, Y., Jiang, J., Yang, W., Jönsson, P.G., 2020a. Magnetic bio-activated carbon production from lignin via a streamlined process and its use in phosphate removal from aqueous solutions. Sci. Total Environ. 708, 135069.
Han, T., Yang, W., Jönsson, P.G., 2020b. Pyrolysis and subsequent steam gasification of metal dry impregnated lignin for the production of H2-rich syngas and magnetic activated carbon. Chem. Eng. J., 124902
Ho, Y.-S., McKay, G., 1999. Pseudo-second order model for sorption processes. Process Biochem. 34, 451–465.
Hollister, C.C., Bisogni, J.J., Lehmann, J., 2013. Ammonium, nitrate, and phosphate sorption to and solute leaching from biochars prepared from corn stover (Zea mays L.) and oak wood (Quercus spp.). J. Environ. Qual. 42, 137–144.
2018. Inquiry to Propose Ban on Spreading Sewage Sludge on Farmland and a Phosphorus Recycling Requirement. Government Offices of Sweden..
Li, R., Wang, J.J., Zhou, B., Awasthi, M.K., Ali, A., Zhang, Z., Lahori, A.H., Mahar, A., 2016. Recovery of phosphate from aqueous solution by magnesium oxide decorated magnetic biochar and its potential as phosphate-based fertilizer substitute. Bioresour. Technol. 215, 209–214.
Li, X., Wang, C., Zhang, J., Liu, J., Liu, B., Chen, G., 2020. Preparation and application of magnetic biochar in water treatment: a critical review. Sci. Total Environ. 711, 134847.
Long, F., Gong, J.-L., Zeng, G.-M., Chen, L., Wang, X.-Y., Deng, J.-H., Niu, Q.-Y., Zhang, H.-Y., Zhang, X.-R., 2011. Removal of phosphate from aqueous solution by magnetic Fe–Zr binary oxide. Chem. Eng. J. 171, 448–455.
Lu, W., Shen, Y., Xie, A., Zhang, W., 2010. Green synthesis and characterization of superparamagnetic Fe3O4 nanoparticles. J. Magn. Magn Mater. 322, 1828–1833.
Luyckx, L., Geerts, S., Van Caneghem, J., 2020. Closing the phosphorus cycle: multi-criteria techno-economic optimization of phosphorus extraction from wastewater treatment sludge ash. Sci. Total Environ. 713, 135543.
Micháleková-Richveisová, B., Frišták, V., Pipíška, M., Ďuriška, L., Moreno-Jimenez, E., Soja, G., 2017. Iron-impregnated biochars as effective phosphate sorption materials. Environ. Sci. Pollut. Control Ser. 24, 463–475.
Nyenje, P., Foppen, J., Uhlenbrook, S., Kulabako, R., Muwanga, A., 2010. Eutrophication and nutrient release in urban areas of sub-Saharan Africa—a review. Sci. Total Environ. 408, 447–455.
Qambrani, N.A., Rahman, M.M., Won, S., Shim, S., Ra, C., 2017. Biochar properties and eco-friendly applications for climate change mitigation, waste management, and wastewater treatment: a review. Renew. Sustain. Energy Rev. 79, 255–273.
Qiu, H., Lv, L., Pan, B.-c., Zhang, Q.-j., Zhang, W.-m., Zhang, Q.-x., 2009. Critical review in adsorption kinetic models. J. Zhejiang Univ. - Sci. 10, 716–724.
Satya Sai, P., Krishnaiah, K., 2005. Development of the pore-size distribution in activated carbon produced from coconut shell char in a fluidized-bed reactor. Ind. Eng. Chem. Res. 44, 51–60.
Vikrant, K., Kim, K.-H., Ok, Y.S., Tsang, D.C., Tsang, Y.F., Giri, B.S., Singh, R.S., 2018. Engineered/designer biochar for the removal of phosphate in water and wastewater. Sci. Total Environ. 616, 1242–1260.
Wang, L., Wang, J., He, C., Lyu, W., Zhang, W., Yan, W., Yang, L., 2019. Development of rare earth element doped magnetic biochars with enhanced phosphate adsorption performance. Colloid. Surface. Physicochem. Eng. Aspect. 561, 236–243.
Wilfert, P., Kumar, P.S., Korving, L., Witkamp, G.-J., van Loosdrecht, M.C., 2015. The relevance of phosphorus and iron chemistry to the recovery of phosphorus from wastewater: a review. Environ. Sci. Technol. 49, 9400–9414.
Yan, L.-g., Yang, K., Shan, R.-r., Yan, T., Wei, J., Yu, S.-j., Yu, H.-q., Du, B., 2015. Kinetic, isotherm and thermodynamic investigations of phosphate adsorption onto core–shell Fe3O4@ LDHs composites with easy magnetic separation assistance. J. Colloid Interface Sci. 448, 508–516.
Zhang, S., Min, Z., Tay, H.-L., Asadullah, M., Li, C.-Z., 2011. Effects of volatile–char interactions on the evolution of char structure during the gasification of Victorian brown coal in steam. Fuel 90, 1529–1535.
Zhang, P., Sun, H., Yu, L., Sun, T., 2013. Adsorption and catalytic hydrolysis of carbaryl and atrazine on pig manure-derived biochars: impact of structural properties of biochars. J. Hazard Mater. 244, 217–224.
Zhang, C., Li, Y., Wang, F., Yu, Z., Wei, J., Yang, Z., Ma, C., Li, Z., Xu, Z., Zeng, G., 2017. Performance of magnetic zirconium-iron oxide nanoparticle in the removal of phosphate from aqueous solution. Appl. Surf. Sci. 396, 1783–1792.
Zhang, C., Shao, Y., Zhang, L., Zhang, S., Westerhof, R.J., Liu, Q., Jia, P., Li, Q., Wang, Y., Hu, X., 2020. Impacts of temperature on evolution of char structure during pyrolysis of lignin. Sci. Total Environ. 699, 134381.